

Fatigue behaviour of M2 and M42 high speed steel up to the gigacycle regime

Ch. R. Sohar¹, A. Betzwar-Kotas², Ch. Gierl¹, B. Weiss², H. Danninger^{1*}

¹*Institute of Chemical Technologies and Analytics, Vienna University of Technology, Getreidemarkt 9/164-CT, Vienna 1140, Austria*

²*Nanostructured Materials-Micromaterials, Faculty of Physics, University of Vienna, Boltzmannngasse 5, Vienna 1090, Austria*

Received 14 May 2008, received in revised form 15 April 2009, accepted 22 April 2009

Abstract

The fatigue behaviour of two ingot metallurgy high speed steels – M2 and M42/Böhler S600 and S500, respectively – was investigated up to $N_{\max} = 10^{10}$ loading cycles employing an ultrasonic frequency resonance testing system in fully reversed tension-compression mode. Testing was done parallel to the rolling direction. Fatigue failure in the tested cycle number range of 10^5 to 10^{10} cycles occurred at stress amplitudes between 900 and 500 MPa, respectively. Failure was initiated at internal carbide clusters, internal and subsurface non-metallic inclusions, and at primary carbides/carbide clusters located at/near the specimen surface, the latter of which represented the dominant failure mode. The obtained *S-N* curves revealed a continuous downward slope without any indication for a plateau region, and hardly any difference was observed between the two steels. In case of internal and subsurface failures the fracture surfaces revealed so-called fish-eye patterns formed around the crack origins. For at/near surface failures, half of fish-eye could be observed. In the vicinity of the crack nucleation site a granular area was detected followed by a fracture surface zone showing rather low surface roughness, thus appearing dark in the scanning electron micrographs.

Key words: tool steels, gigacycle fatigue, ultrasonic frequency fatigue testing, non-metallic inclusions, primary carbides clusters, fish-eye patterns

1. Introduction

Typical applications of high-speed tool steels are all types of cutting tools such as drills, mills, milling cutters, metal saws, but also cold work tools such as die inserts, tread-rolling dies, punching and blanking dies. These applications have in common high number of loading cycles during service during which the tools are exposed to cyclic stresses and strains, and thus, as a consequence, tools fail not only due to wear of the cutting edges but also to – mechanical and/or thermal – cyclic loading. In low cycle fatigue, failure of materials occurs due to crack initiation at surface defects such as machining flaws or persistent slip bands, non-metallic inclusions located at the surface or at holes originating from decohesion of inclusions. The fatigue behaviour beyond 10^6 cycles became a focus

of investigation after Naito et al. [1] had shown in 1984 that carburized and surface hardened steels did not exhibit a conventional fatigue limit at 10^6 to 10^7 cycles and failed even beyond 10^7 loading cycles at fairly low stresses applied. This phenomenon was observed predominantly for high strength bearing and spring steels, for which numerous studies on the fatigue behaviour [2–27] were published during the last two decades. The present authors [28] gave a review of the existing literature in a recently published article, in which the influence of the loading type and the test frequency and also the effect of residual stresses on the fatigue behaviour were discussed. Summarizing, the frequency effect on fatigue behaviour was claimed to be negligible [2, 8, 29]. However, the influence of the loading mode cannot be denied since rotating bending fatigue tests usually exhibit so-called ‘duplex’ or

*Corresponding author: tel.: +431 58801 16400; fax: +431 58801 16499; e-mail address: hdanning@mail.tuwien.ac.at

‘multi-step’ S - N curves while in tension-compression tests such a stepwise shape was found by Wang et al. [3] only. Murakami et al. [14] attributed this different appearance of the S - N curves to the smaller test volume and to the stress gradient occurring in rotating bending tests, which was also suggested by Marines et al. [2]. However, the most important conclusion of all the studies cited above is that these high strength steels fail also at stress levels below the conventional “fatigue limit”, in the long life regime above 10^7 loading cycles. Usually failure of these steels in the very high cycle fatigue regime is associated with internal crack initiation and so-called fish-eye patterns at the fracture surface. Crack origins of internal failures were found to be mostly non-metallic inclusions, such as Al_2O_3 , TiN, SiO_2 , MgO, and CaO, or sulphides. Furthermore, it has been reported that the area around the internal crack origin plays a critical role in the gigacycle fatigue mechanism. Murakami et al. [15] introduced the term “optically dark area” (ODA) for this zone that appeared dark in the light optical microscope, which they claimed to be formed due to a synergistic effect of cyclic loading and hydrogen environment. There exist also other designations for this area in the literature such as “rough surface area” (RSA) [20], “fine granular area” (FGA) [21], “granular bright facet” (GBF) [23, 25], “facet” (FCT) [26], or granular (bright) area, as called by the present authors [30].

Concluding it has to be mentioned here that the number of fatigue data investigating the fatigue behaviour beyond 10^7 loading cycles is rather limited compared to the data available in the standard-cycle fatigue regime ($< 10^7$ cycles), predominantly due to time (and thus financial) constraints at usual test frequencies. Also the range of high strength steels that have been under investigation so far is rather small. This holds especially for tool steels, which differ from high strength bearing and spring steels in such a way that tool steels contain numerous primary carbides required for high abrasion resistance, often in the same size or larger as the aforementioned crack initiating inclusions, and thus, the amount of “defects” is several magnitudes higher than for the materials discussed above. Investigations of fatigue behaviour of tool steels are scarce and mostly limited to maximum cycle numbers of 10^6 to 10^7 [28, 30–37]. Summarizing the existing studies up to 10^7 loading cycles [31–36], crack origins were found to be non-metallic inclusions, but also primary carbides and carbide aggregates, which were located in the interior or within the surface layer of the specimen. Recently, the present authors [28, 30, 37] studied the gigacycle fatigue behaviour of AISI D2 type cold work tool steel, and it was found that primary carbides and carbide clusters located in the interior and at/near the surface caused fatigue failure. It has been shown that the existence of compressive

residual stresses at the specimen surface heavily influences the SN data and the location of crack origin [28]. Furthermore, considerably anisotropic fatigue behaviour [37] of the studied wrought D2 tool steel was observed.

There are two major reasons why the fatigue behaviour of tool steels, also up to very high cycle numbers, is of high interest: First, service operations impose a repeated exposure to stresses and strains due to the contact between tool and workpiece, and secondly, fatigue testing at low stresses up to the gigacycle fatigue regime represents a reasonable tool for identifying defects, especially singularities, in the studied material. Furuya et al. [9] propose that fatigue testing employing a 20 kHz ultrasonic fatigue testing system is a novel method for the inspection of inclusions in low-alloy spring steels, arguing that this inspection method is superior to conventional scanning of polished surfaces, especially for low numbers of small inclusions. Since users of tool steels demand closer tolerances and finer surface finish for continuous improvement of the material properties, especially with respect to reliability and lifetime, several processes to improve the steel quality have been introduced over the recent decades. Special refining processes such as electro slag re-melting are nowadays state of the art in the production of ingot metallurgy tool steels, which techniques decrease the amount of slag impurities significantly. However, in absence of these impurities larger carbides and carbide agglomerations, which are generated during the solidification process, represent potential failure origins. It is obvious that detailed knowledge of potential crack initiation sites is required for further improvement of tool steel performance.

The work presented here aims at providing S - N data up to $N_{\max} = 10^{10}$ cycles for two high speed tool steels produced by ingot metallurgy, and revealing potential crack initiating defects, employing an ultrasonic frequency fatigue testing system that operates at 20 kHz in fully-reversed push-pull mode ($R = -1$), since this method overcomes the time constraints of usual testing set-ups such as rotating bending machines or servo-hydraulic tension-compression devices, thus offering the possibility of fast and accurate detection of potential material defects, especially of singularities.

2. Experimental

In this study the fatigue behaviour of two high-speed steels – AISI grades M42 and M2 – produced by conventional ingot metallurgy was investigated. Both steels were acquired from *Böhler Edelstahl GmbH*, Austria (Böhler grades S500 and S600, respectively), supplied as annealed cylindrical bars with a diameter of 15.5 and 20.5 mm, respectively. Chemical composi-

Table 1. Chemical composition (mass%) of the studied high speed tool steels

Steel	AISI	C	Si	Mn	Cr	Mo	V	W	Co	Ni	S	P
S500 (HS 2-10-1-8)	M42	1.1	0.52	0.23	4.2	11.0	1.0	1.9	8.1	0.2	0.002	0.018
S600 (HS 6-5-2)	M2	0.9	0.35	0.30	4.3	4.8	2.2	6.1	0.7	0.5	–	–

tion as derived from X-ray fluorescence analysis – except the carbon content, which was taken from the manufacturer product information – is shown for the major constituents in Table 1. The two steels differ in the carbon, tungsten and molybdenum concentration. Steel S500 (HS 2-10-1-8, M42) is molybdenum-rich high-speed steel, containing a considerable amount of cobalt, which improves the red hardness. Furthermore, small amounts of Cr, W and V are also present in this steel. Steel S600 (HS 6-5-2, M2) is molybdenum-tungsten-based high-speed steel, which contains almost identical mass% of the two strong carbide forming elements W and Mo. Carbon content is somewhat lower, and the steel S600 contains slightly more vanadium, but no cobalt.

All fatigue test specimens were prepared for fatigue loading in the rolling direction, i.e. in the favourable microstructural orientation of these anisotropic materials. The round bars were turned to the desired geometry similar to that proposed for the cold work steel tested recently [28], and their surface was longitudinally ground prior to the heat treatment in such a way that the specimen slowly rotated while it was polished parallel to the specimen axis by a rapidly rotating disk. The rotating disk was spring mounted in order to avoid undesired pressure on the sample, which might induce stresses in the material. Steel S500 was then austenitized at 1190 °C for 25 min and quenched in oil. Subsequently, three times tempering was done at 610, 610 and 570 °C, respectively, for 2 hours each, followed by slow cooling. In case of steel S600 the austenitizing temperature was 1200 °C, and three times tempering was performed at 610, 610 and 580 °C. The heat treatment parameters have been defined according to the recommendations given by the steel manufacturer. All heat treatments were carried out in a push-type laboratory furnace with gas-tight superalloy retort under high purity nitrogen atmosphere (5.0 N₂). The heat treated hour glass shaped fatigue specimens were then polished to mirror-like finish in the longitudinal direction using 240 mesh aluminium oxide abrasive paper, 15 µm, 6 µm, and 1 µm diamond suspension, similar to the grinding accomplished prior to the heat treatment as described above. Polishing using 15 µm diamond suspension was applied for material removal in order to eliminate grinding-induced surface compressive residual stresses, material up to a depth of 150 µm being removed [28].

Rockwell C hardness measurements were per-

formed at an *EMCO testing device (M4U-025)* at each fatigue specimen for sake of quality control. Microhardness was measured on a *Leco LM 100 testing system* at a load of 0.25 N. Furthermore, transverse rupture strength (TRS) was determined on round samples with 6 mm diameter and a length of 80 mm with surface finish using 600 mesh SiC abrasive paper by three-point bending test on a *Zwick 1474* universal testing machine. The dynamic Young's modulus was measured on specimens ground to rectangular shape (100 × 10 × 10 mm) using a *Grindosonic* resonance frequency measurement system. Residual stresses have been measured at the surface in the narrowest section of the fatigue samples, employing X-ray diffraction and the $\sin^2 \Psi$ -method [Cr K α , $\theta = 78.06^\circ$, lattice plane: {211}, $1/2 S_2 = 6.09 \times 10^{-6}$]. For fatigue testing an ultrasonic testing system (*Telsonic-Ultrasonics*) operating at 20 kHz in fully reversed mode ($R = -1$) was employed, details of which have been presented recently [28]. The probability of cavitation and corrosion due to the specimen cooling, which was required due to the heat developed within the samples during fatigue testing, was thoroughly discussed previously [28]. It was concluded that these effects were negligible. Light microscopic investigations were accomplished on an *Olympus light microscope GX51F*. Image analyses were performed using a commercial software package (*analySIS Vers. 5.0 from Soft Imaging System GmbH, Germany*) and an open source software (*ImageJ 1.37v from National Institute of Health, USA*). Fracture surfaces were examined by means of scanning electron microscopy (*FEI Quanta 200*).

3. Material characterization

3.1. Microstructure

The light optical micrograph (LOM) of the as-quenched microstructure transverse to the rolling direction of the initial S500 steel bar is presented in Fig. 1, in which prior austenite grain boundaries are visible showing that there was no undesirable grain growth. The prior austenite grain size was determined using the Snyder-Graff method, and it turned out to be $10 \pm 1 \mu\text{m}$ and $11 \pm 1 \mu\text{m}$ for steel S500 and S600, respectively, for the applied austenitizing conditions. The transverse microstructure after three times tempering is shown in Fig. 2 for steel S500.

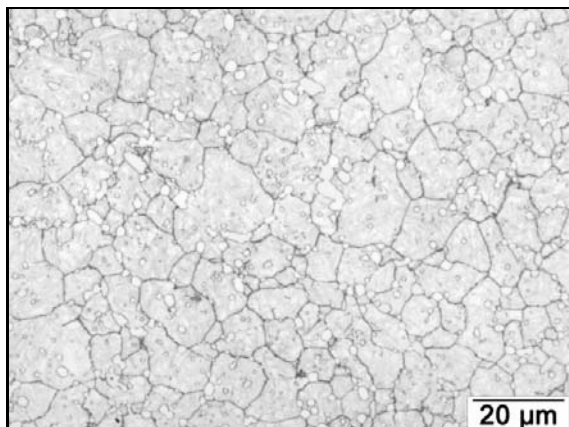


Fig. 1. As-quenched microstructure of steel S500/M42 (LOM, etched with 5 % Nital, 1000 \times).

Short etching with 5 % Nital (Fig. 2a,c,d) revealed nicely the tempered martensitic structure and partly the prior austenite grain boundaries. Backscattered electron images (BSE) revealed the fine needle struc-

ture of tempered martensite, and primary carbides (white phases) were located predominantly at the grain boundaries. Fine martensitic needle structure was observed within the grains (Fig. 2d). X-ray diffraction (XRD) proved that retained austenite had been more or less completely transformed upon three times tempering. Electron probe microanalysis (EPMA) of the martensitic matrix revealed that some Mo, Cr, and more Co were in solid solution in the iron matrix of the S500 steel after the applied heat treatment. Two types of primary carbides can be distinguished in Fig. 2b due to different etching behaviour by Murakami's agent. Mo-rich M_6C type carbides were attacked, whereas V-rich MC carbides remain white. However, the MC particle borders are attacked by the etchant. EPMA further confirmed that M_6C type carbides contained predominantly Mo for steel S500. In case of S600 similar amounts of W and Mo were found in M_6C type carbides. MC type carbides revealed high V content. Furthermore, XRD proved the existence at least of the M_6C carbides. The content of MC carbides was too low for detection by XRD. In the transverse section – which corresponds to the direction of the ob-

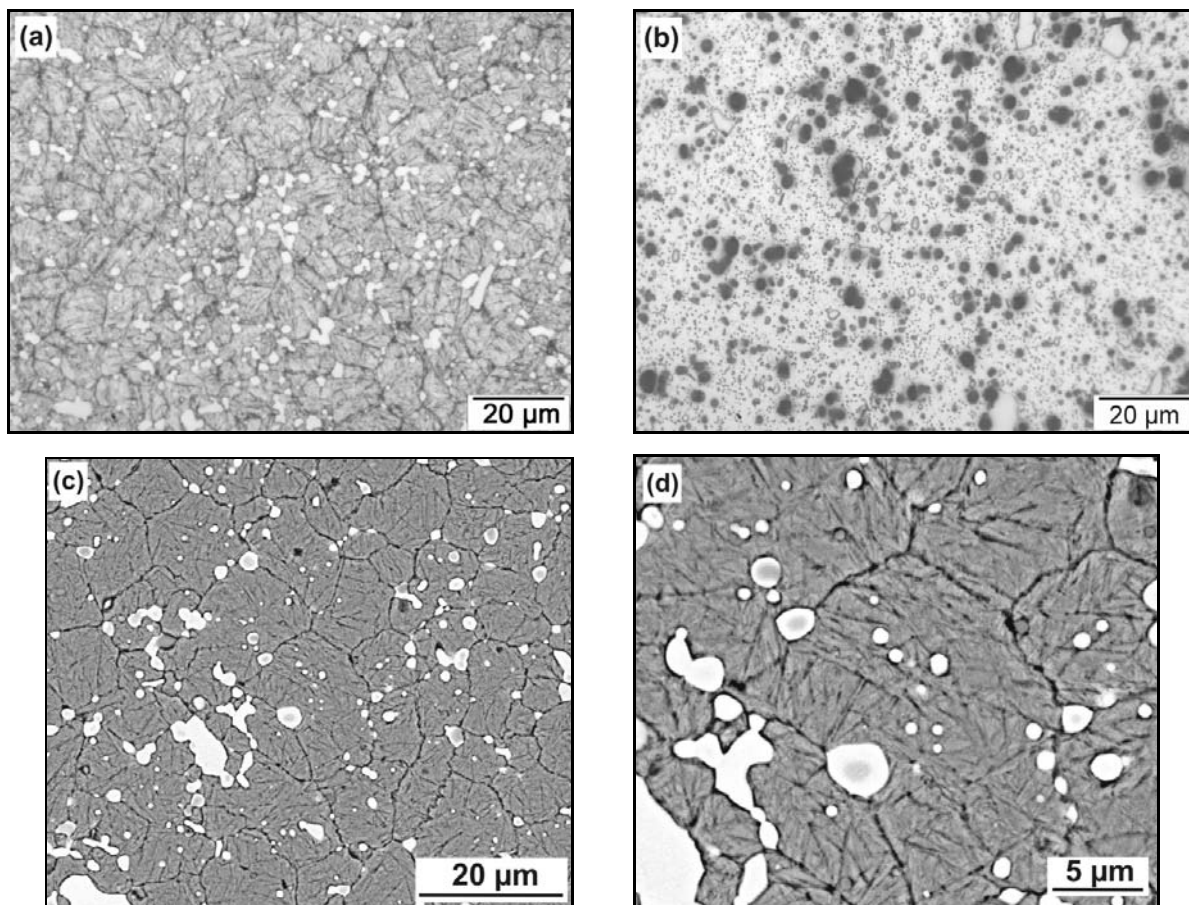


Fig. 2. Transverse microstructure of steel S500/M42, quenched and 3 \times tempered: (a) LOM, Nital, (b) LOM, Murakami and (c, d) backscattered electron images.

Table 2. Mechanical properties of the studied high-speed steels

Steel	Rockwell Hardness HRC 150 kg		T.R.S. (MPa)	Dynamic Young's Modulus (GPa)
	as-quenched	tempered	tempered steel	tempered steel
"S500"/M42	58 ± 2	66 ± 2	3400 ± 250	207 ± 7
"S600"/M2	64 ± 2	64 ± 2	3600 ± 400	208 ± 6

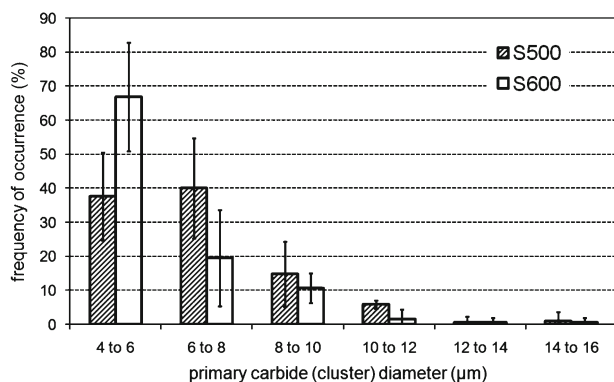


Fig. 3. Classification of primary carbides according to their size.

tained fracture surfaces – the carbide distribution was rather homogeneous. However, in the longitudinal section – parallel to the rolling direction of the steel bar – primary carbide bands were observed, as characteristic for ingot metallurgy tool steels. The volume fraction of primary carbides in tempered steel was determined in the cross section using image analysing software applied on 18 optical micrographs at 500× and 1000× magnification. It turned out to be 7 ± 1 vol.% and 6 ± 2 vol.% for steels S500 and S600, respectively. Furthermore, measuring of the primary carbide particle sizes in as-heat treated steel was performed using LOM images at magnification 1000×, 6 images each. The classification in the transverse section according to the primary carbide Feret diameter is presented in Fig. 3 for both steels. Obviously, the largest observed carbide species had a diameter $< 20 \mu\text{m}$, which is rather small compared e.g. to the chromium carbides of cold work tool steel K110 [28]. Considering the scatter of the data, S500 and S600 primary carbide sizes were rather similar, which holds also for the observed microstructures of steel S600. Non-metallic inclusions have not been detected in metallographic investigations for S500 steel. In contrast, in case of steel S600 some inclusions were observed.

3.2. Mechanical properties

Rockwell hardness, dynamic Young's modulus and transverse rupture strength (TRS) were measured

(Table 2). In the as-received (annealed) condition the steel S500 had a hardness of about 22 HRC. Steel S600 had a higher annealed hardness of about 26 HRC due to the higher W content, which holds also for the as-quenched hardness. In case of steel S500, significant hardness increase was observed during tempering, which was attributed to the secondary hardening effect in Mo-based high-speed steels. The TRS and dynamic Young's moduli of both high-speed steels were rather similar.

3.3. Residual stresses

XRD measurements showed that after removal of about $150 \mu\text{m}$ from the surface by polishing, as described in the experimental section, compressive residual stresses in the range of -120 to -190 MPa were present at the surface in the narrowest section of the specimen.

4. Results and discussion

4.1. $S-N$ data

Figure 4a shows the obtained $S-N$ data for steel S500. The types of crack origin are specially marked, and in addition the graphs for 10, 50, and 90 % fracture probability are also presented. The fatigue strength decreases by half from 850 MPa at 10^5 loading cycles to 450 MPa at 10^{10} loading cycles, where three runout specimens (\blacktriangle , $N_{\text{max}} = 10^{10}$ cycles) were obtained. In addition, at 500 MPa one further runout sample (\blacktriangle) was obtained, however, at this stress amplitude three other samples failed after about 10^8 cycles. Obviously, the observed scatter of the data was rather small. Two specimens, which were preliminary samples and failed at surprisingly long lives at 900 MPa, are assumed to have had significantly higher initial surface residual stresses compared to the rest of the specimens, since residual stress measurement at specimen ground and polished similarly to these two specimens revealed compressive stresses at the surface in the range of -400 MPa, which probably inhibited or delayed the crack initiation at the surface (see [28]). Five different types of crack origins were observed: At higher amplitudes, internal failures ori-

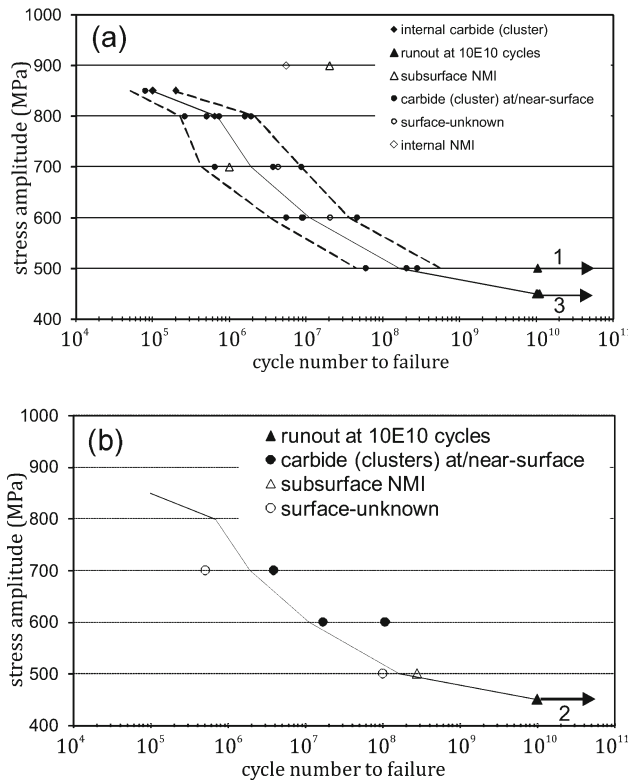


Fig. 4. (a) *S-N* data of steel S500 – the solid and the two dashed lines represent 50 %, 10 % and 90 % fracture probability, respectively, (b) *S-N* data of steel S600 – the solid line represents 50 % fracture probability of steel S500 (figures close to the arrows indicate the number of run-out specimens).

ginated at internal carbides (◆) and, in some cases, at a non-metallic inclusion (◇) forming so-called fish-eye patterns at the fracture surfaces. Furthermore, two subsurface failures due to large non-metallic inclusions (△) with diameters about 73 and 33 μm , respectively, were found, which confirms Furuya's statement that by gigacycle fatigue testing, non-metallic inclusions are found that are hardly detectable in metallography. The major part of the failed specimens showed fatigue crack initiation at primary carbides and carbide clusters located at or close to the surface (●). For a few samples (○) it was impossible to identify the crack origins; however, the fatigue cracks definitely started within the surface region.

Fatigue behaviour of steel S600 (Fig. 4b) was similar to steel S500. Fatigue tests of steel S600 were done for a few specimens at stress amplitudes of 700, 600, 500 and 450 MPa, two samples each, and sample failures occurred within the confidence band obtained for steel S500. Crack initiation was found to take place at primary carbides or carbide clusters located at/near the surface and at subsurface non-metallic inclusions, as described above for steel S500. However, internal failures were not observed here, probably due to the

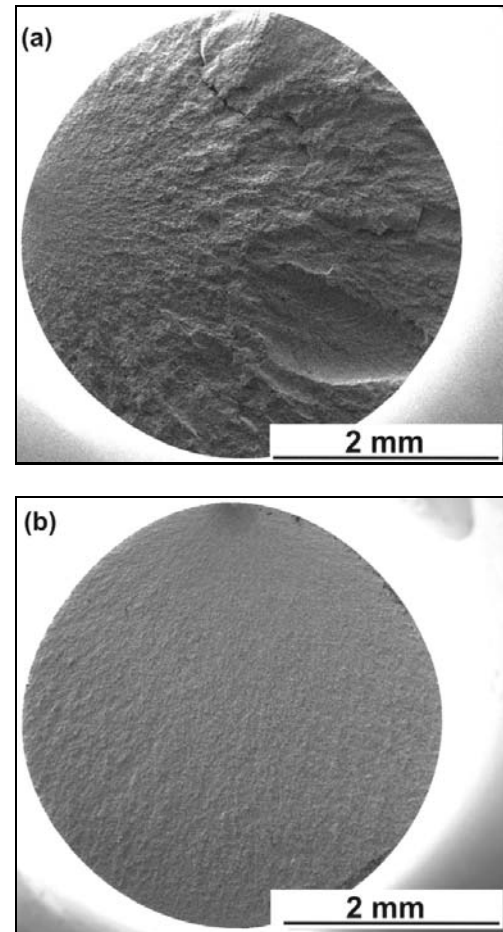


Fig. 5. Macroscopic fracture surface of (a) S500 specimen failed after 5.0×10^5 cycles at 800 MPa and (b) S600 specimen failed after 3.9×10^6 cycles at 700 MPa.

limited number of specimens tested. Furthermore, two run-outs were obtained at 450 MPa after 10^{10} cycles; thus, the fatigue strength at 10^{10} loading cycles was similar to that obtained for steel S500.

Comparing the fatigue data of the two high speed steels S500 and S600 to the data obtained for AISI D2 type wrought cold work tool steel (Böhler grade K110), which has been presented recently [28], it surprisingly turned out that the gigacycle fatigue behaviour of these steels was similar in case of low residual stresses at the specimen surface, despite the fact that the hardness of the high speed steels was about 8 HRC higher than that of the cold work steel. However, it has to be considered that the TRS and Young's moduli are similar, too. Consequently, it seems that the elastic behaviour and the ductility of the matrix have a more pronounced influence on the fatigue behaviour than the hardness, which is predominantly determined by the very hard W and Mo carbides. For both steel types, primary carbides

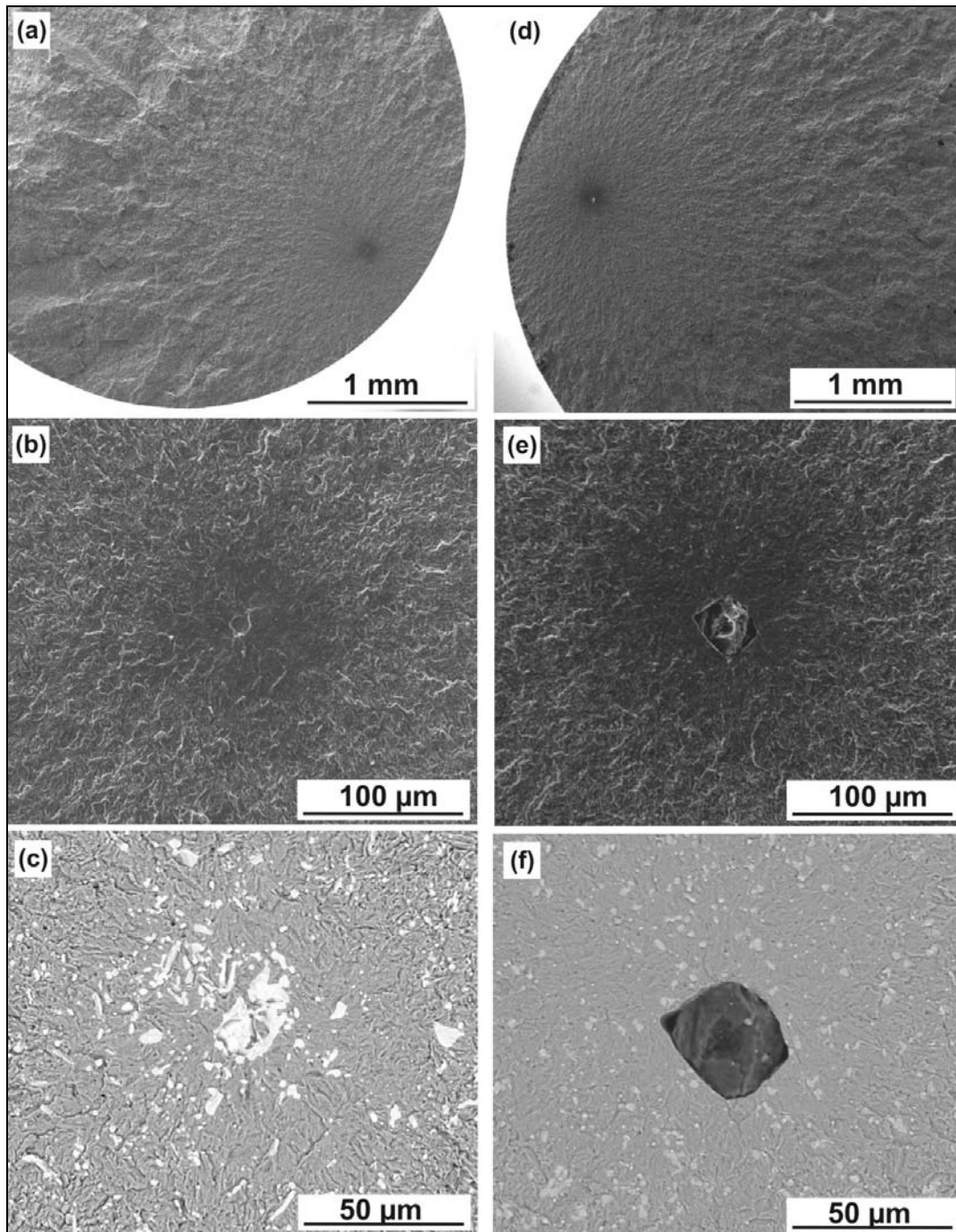


Fig. 6. Representative fractographs of internal failures of steel S500. (a, b, c) Specimen failed at 850 MPa after 1×10^5 cycles from primary carbide cluster; (d, e, f) Specimen failed at 900 MPa after 5.5×10^6 cycles from a non-metallic inclusion.

and carbide clusters at/near the surface represent the most important group of fatigue crack origins, if low residual stresses exist at the specimen surface. Furthermore, for steel K110 it turned out that high compressive surface residual stresses shifted the $S-N$ curve towards longer specimen lives, and specimens failed due to internal carbide clusters

in the cycle number range of 10^5 to 10^7 . As described above, two specimens of steel S500 failed at 900 MPa at significantly longer lives, probably due to high compressive stresses at the specimen surface, which is corroborated by the fact that K110L-I specimens (high compressive stresses) revealed similar fatigue lives and showed also internally induced failure.

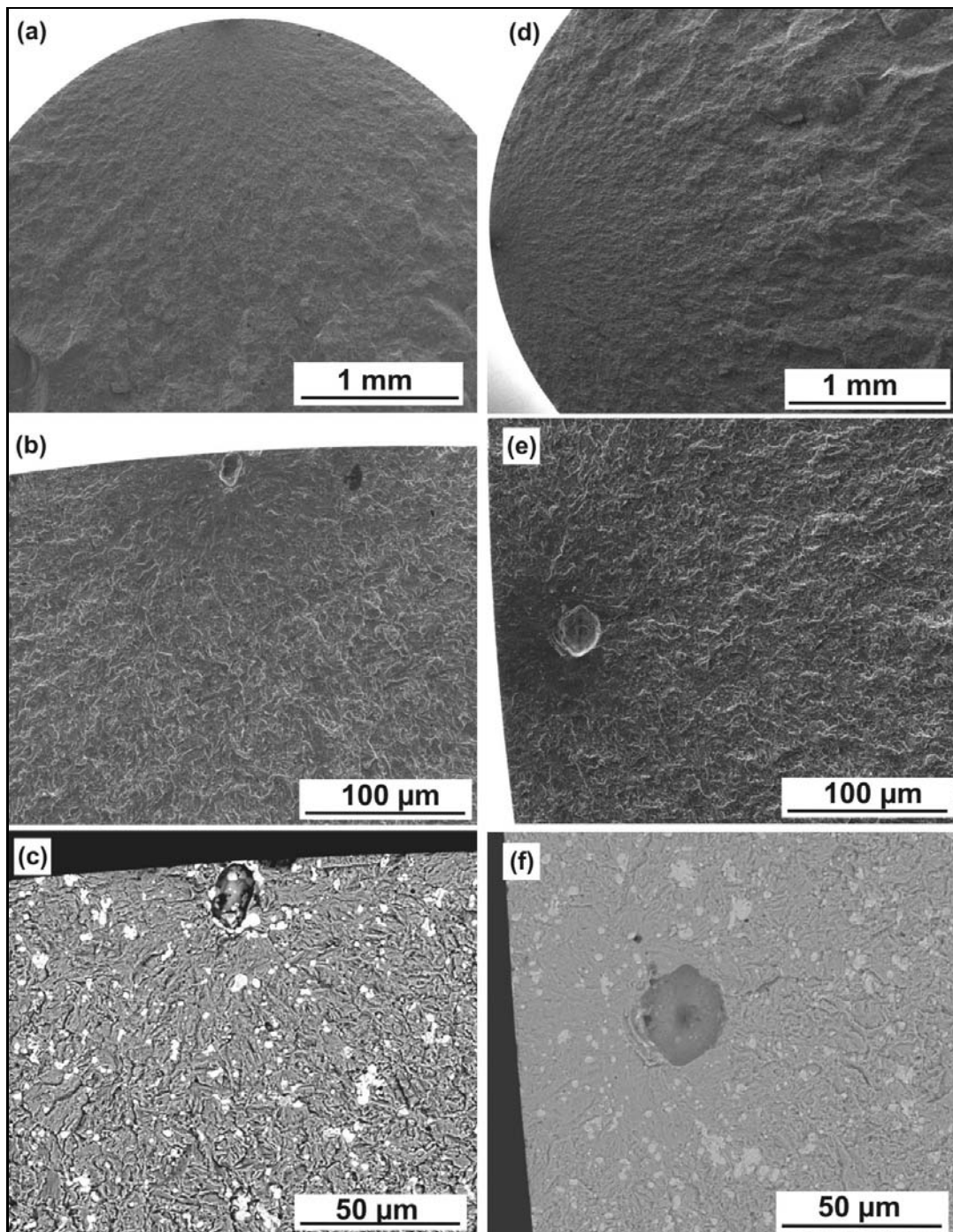


Fig. 7. Representative fractographs of at/near-surface (a, b, c) and subsurface failures (d, e, f) of steel S500: (a, b, c) Specimen failed due to large primary carbide at 800 MPa after 2.6×10^5 cycles; (d, e, f) Specimen failed at 900 MPa after 2×10^7 cycles due to a subsurface non-metallic inclusion.

4.2. Fractography

Macroscopically, the obtained fracture surfaces of steel S500 and S600 looked very much the same as those obtained for AISI D2 type wrought cold work tool steel [28, 30, 37], regardless of the type of crack origin. However, especially at high stress amplitudes part of the fracture surfaces of the two high speed

steels studied here exhibited areas with high edges and ridges (Fig. 5a), probably derived from an overload during final fracture of the specimen. The area of this part of the final fracture surface decreased considerably with increasing sample life and totally disappeared at lower stress amplitudes (Fig. 5b).

Fracture surfaces on the microscopic level revealed up to two zones within the (half) fish-eye pattern,

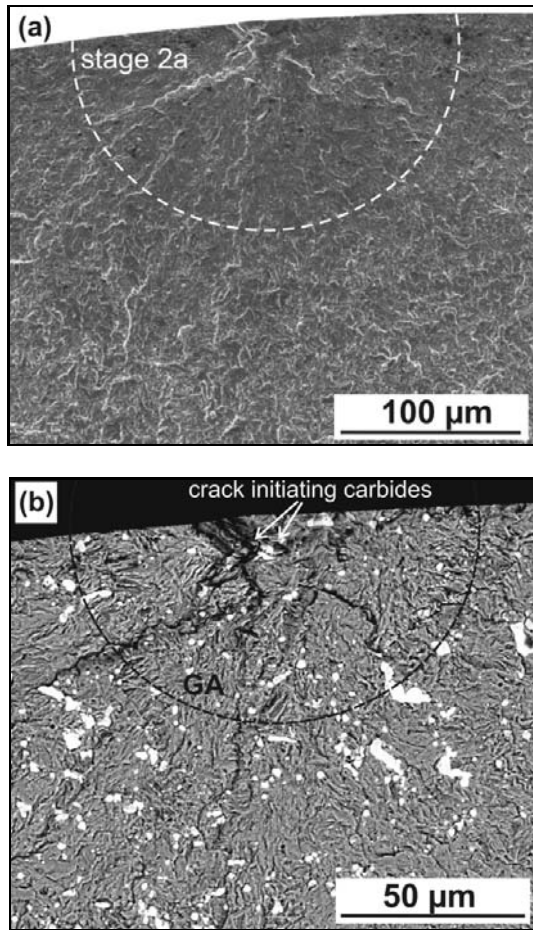


Fig. 8. Fracture surface of S500 specimen failed due to closely arranged primary carbides at 500 MPa after 5.2×10^8 loading cycles: (a) SEM image showing zone with rather low surface roughness (stage 2a), (b) BSE image revealing the crack origin and the surrounding granular area (GA).

depending on the type of crack origin and applied stress amplitude. In contrast, fracture surfaces of cold work tool steel showed five different zones of crack growth in case of internal failure [30]. Here, for the two high-speed steels fish-eye or half-fish-eye-like pattern (see Figs. 6 and 7) was formed around the internal and at/near-surface crack origin, respectively, of which however, exact definition of the borderline to final fracture surface was difficult since a rather gradual change of the structure was observed. In the vicinity of the crack origin (see Fig. 8), except for cases in which a non-metallic inclusion initiated the fatigue crack, an area exhibiting a granular surface morphology (GA in Fig. 8b) was observed, especially at longer fatigue lives, as described recently for D2 [30, 37]. However, in contrast to those studies on D2 [30, 37], for the two high speed steels studied here the granular surface morphology was by far not as pronounced, and an exact determination of the size of this

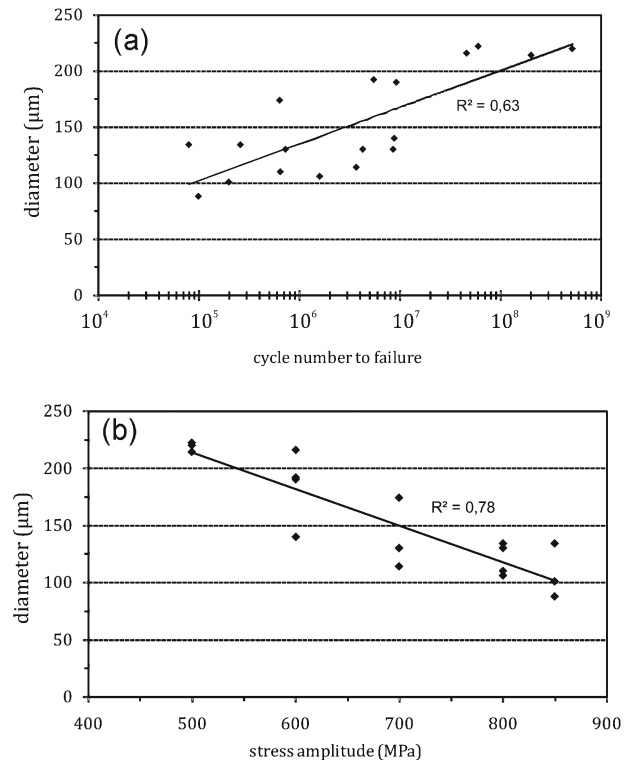


Fig. 9. Relationship between radius of crack growth stage 2a, (a) cycle number to failure, and (b) applied stress amplitude.

granular area (GA) was not possible. Furthermore, it seems that a gradual change from the granular area to the subsequent crack growth stage occurred. This subsequent area, called “stage 2a”, is characterized by a rather low surface roughness and thus appears dark in the SEM (Fig. 8a). It is speculated that the low surface roughness might be due to the very slow crack growth here, which can be supposed to result in crack growth exactly perpendicular to the stress orientation. Since it can be assumed that crack growth in this region is rather slow, a large proportion of fatigue life is spent there. The transition from stage 2a to the subsequent crack propagation process seems to be fairly continuous. Outside of area 2a, crack growth is assumed to be relatively fast; consequently the surface roughness is fairly high. The size of the stage 2a area showed a direct relationship with the cycle number to failure (Fig. 9a), which was also observed in recent studies [30, 37]. Consequently, the longer the specimen lives, the larger the stage 2a area is, which means that a significant part of the specimen life is spent within this crack growth zone, which presumably corresponds to short crack growth. Furthermore, it turned out that the lower the applied stress amplitude, the larger the observed size of stage 2a was (Fig. 9b).

4.3. Fatigue crack initiation (CI)

Four types of crack origins have been identified (except for a few specimens, for which the determination of the crack initiation site was not possible). The four CI types can be categorized into internal and surface/subsurface failures. Figure 6 shows characteristic internal failures starting from a carbide cluster (Fig. 6a–c) and a non-metallic inclusion (Fig. 6d–f). The primary carbides appear bright in the BSE image due to the high atomic number. In contrast, the non-metallic inclusions appear dark due to their lower atomic mass. While the non-metallic inclusion is rather isolated, numerous somewhat smaller carbides closely arranged to each other surround the large primary carbide. This constellation seems to be a prerequisite for internal crack formation from primary carbides, since this arrangement might offer highest stress concentration due to superposition of the stress fields of the individual carbides, probably causing cracking of the carbides. In most cases the hard primary carbides fractured rather than decohering from the matrix, thus, they were observed on both mating fracture surfaces. Only in a few cases a hole was observed at one fracture surface while on the mating surface a carbide particle turned out to be the crack origin. The latter indicates that the crack proceeded around the initiating carbide particles, which were M_6C type carbides, Mo-rich and W-Mo-rich in steel S500 and S600, respectively. The diameters of the carbide clusters that caused internal failure ranged from 30 to 40 μm . According to electron probe microanalysis, the non-metallic inclusions contained large amounts of Ca, Al, Mg, and oxygen, and were somewhat larger, i.e. 30 to 75 μm , than the internal carbide clusters. Thus it can be assumed that the inclusions were typical slag impurities such as CaO, MgO and Al_2O_3 . Distances of the internal crack origins to the specimen surface, which ranged from 380 to 1800 μm , revealed a relationship neither to the applied stress amplitude nor to the cycle number to failure. Thus it can be concluded that these internal defects represented singularities within the tested material volume. Since the number of specimens that failed due to internal and subsurface defects was too low, correlating with applied stress amplitude and cycle number to failure would not be meaningful.

Figure 7 shows characteristic crack origins of fatigue failure from primary carbides located at or close to the specimen surface (Fig. 7a–c) and from subsurface non-metallic inclusions (Fig. 7d–f). In contrast to internal failures, subsurface crack origins revealed fish-eye patterns, the border of which touches the specimen surface. In case of at/near surface failure, half of fish-eye is formed, showing a similar dark surface area in the vicinity of the carbide aggregates as described before. The determination of crack origins

at/near the surface was difficult in many cases since it seemed that during final fracture or during compressive cycles the surface region in the vicinity of the crack origin was destroyed, which had been reported earlier [28, 35]. However, identification of the crack origin was totally impossible only for a few samples. Other possible reasons for the observed near-surface failures, such as corrosion and cavitation, have been excluded earlier [28]. The diameters of these at/near-surface crack initiating carbides and carbide clusters ranged from 10 to 60 μm , thus they were in part far larger compared to the maximum carbide sizes obtained in the metallographic investigations. Nevertheless, these large carbide clusters seem to exist in numbers high enough that the probability of occurrence at/near the specimen surface is high, thus, they do not represent material singularities. An estimation of the location of the crack origin – internal or at/near-surface – can be performed according to the statistical concept presented recently [28]. With increasing “defect” volume content, which means here volume content of potentially crack initiating carbides, the probability that at least one of them is located at/near the surface increases. Consequently, it is essential to calculate a critical carbide volume content, above which surface induced failure will be dominant. Assuming a carbide diameter of 10 μm – which was found to be the smallest crack initiating carbide – and considering the total carbide volume fraction for the two high speed steels, i.e. about 7 %, the critical carbide volume fraction is 3×10^{-6} %, which is by far exceeded by the volume fraction of carbides having a diameter larger than 10 μm (0.56 %) as observed in the metallographic investigations. Thus, the probability of finding such a potential crack initiator at the specimen surface is high and consequently at/near-surface failures are dominant for the two high-speed steels, which is confirmed by the results of the fatigue experiments.

The carbide/carbide cluster size did not reveal any relationship to the applied stress amplitude and cycle number to failure, which agreed with findings for AISI D2 type tool steel [30]. The authors [30] claimed there that the formation of a granular area was a prerequisite for the formation of a short fatigue crack, i.e. when the granular area reached a certain size. Shiozawa et al. [25] proposed that such granular area could be formed around an inclusion according to a model called “dispersive decohesion of spherical carbides”. There, multiple microcracks are formed by the decohesion of the matrix from small spherical carbides, which however is enhanced by stress concentration in the vicinity of larger primary carbides. These microcracks then grow and coalesce to form short fatigue cracks. However, unless an appropriate short crack length – which corresponds to the size of the granular area – is reached, these short cracks are non-propagating cracks. Thus, the described microcrack

formation and coalescence within the granular area take place until a short propagating crack is formed.

For the two high speed steels studied here it can be argued similarly, since also a granular area was observed; however, the appearance of this granular area was not that obvious as it was for the cold work tool steel studied recently. Furthermore, at stress amplitudes > 700 MPa the crack initiating carbides were large enough to trigger a propagating fatigue crack, and thus, it seemed that a granular area was not formed. The fact that no correlation between carbide sizes and applied stress amplitude or cycle number to failure was observed supports the hypothesis that the formation of the granular area is essential for the development of a propagating fatigue crack.

5. Conclusion

Summarizing, fatigue testing of two-ingot metallurgy high-speed steels – M2 and M42 – up to 10^{10} loading cycles revealed the following:

- The two high speed steels studied failed even beyond 10^6 loading cycles at stress amplitudes lower than 900 MPa, showing similar fatigue behaviour. The observed $S-N$ curves, which revealed low scatter, resembled the data recently obtained for high chromium cold work tool steel also at absolute stress levels [28], despite the significant difference of material hardness.

- Crack initiation sites were internal carbides/carbide clusters, internal and subsurface non-metallic inclusions, and primary carbides/carbide clusters located at/near the surface, which represented the dominant group of fatigue crack origins. Crack nucleating carbides were Mo-W-rich (steel S500) and W-rich (steel S600) M_6C type carbides > 10 μm , respectively. For these carbides, fracture was observed rather than decohesion from the matrix, latter effect of which was however observed around non-metallic inclusions, i.e. typical slag impurities such as CaO, MgO and Al_2O_3 .

- Fracture surfaces revealed so-called fish-eye patterns formed around the crack origin in case of internal and subsurface failures. For at/near surface failures, half fish-eye structure was observed. Clear determination of the border of the fish-eye was not possible, which also held for the other crack growth stages identified, since the transition from one crack growth stage to another seemed to occur rather gradually. In the vicinity of the crack initiating carbides a granular area was detected similar to that observed for cold work tool steel [30], however, its appearance was not as pronounced. The subsequent crack growth stage – called stage 2a – was visible more clearly, which was characterized by a dark appearance in SEM and a rather low surface roughness, which can be due to the very slow crack growth there that can be supposed to result in crack growth exactly perpendicular to the stress ori-

entation. Thus it can be speculated that a long period of fatigue life is spent within this crack growth stage.

- The size of crack initiating carbides/carbide clusters did not reveal any relationship with applied stress amplitude/cycle number to failure, at least at amplitudes < 700 MPa, for which carbides/carbide clusters were not large enough to directly initiate a short propagating fatigue crack. However, through the formation and coalescence of numerous microcracks in the vicinity of the primary carbides such a propagating crack might be formed according to the model by Shiozawa et al. [25]. This process results in the formation of a granular area around the crack origin.

Acknowledgements

This project is financially supported by the Austrian Science Fund (FWF project number P17650-N02).

References

- [1] NAITO, T.—UEDA, H.—KIKUCHI, M.: *Met. Trans. A*, 15A, 1984, p. 1431.
- [2] MARINES, I.—DOMINGUEZ, G.—BAUDRY, G.—VITTORI, J.-F.—RATHERY, S.—DOUCET, J.-P.—BATHIAS, C.: *Int. J. Fatigue*, 25, 2003, p. 1037.
- [3] WANG, Q. Y.—BATHIAS, C.—KAWAGOISHI, N.—CHEN, Q.: *Int. J. Fatigue*, 25, 2002, p. 1269.
- [4] FURUYA, Y.—MATSUOKA, S.—ABE, T.: *Met. Mat. Trans. A*, 35A, 2004, p. 3737.
- [5] ABE, T.—FURUYA, Y.—MATSUOKA, S.: *Fatigue Fract. Engng. Mater. Struct.*, 27, 2004, p. 159.
- [6] FURUYA, Y.—MATSUOKA, S.: *Met. Mat. Trans. A*, 35A, 2004, p. 1715.
- [7] FURUYA, Y.—ABE, T.—MATSUOKA, S.: *Fatigue Fract. Engng. Mater. Struct.*, 26, 2003, p. 641.
- [8] FURUYA, Y.—MATSUOKA, S.—ABE, T.—YAMAGUCHI, K.: *Scripta Mater.*, 46, 2002, p. 157.
- [9] FURUYA, Y.—MATSUOKA, S.—ABE, T.: *Met. Mat. Trans. A*, 34A, 2003, p. 2517.
- [10] ITOGA, H.—KO, H.-N.—TOKAJI, K.—NAKAJIMA, M.: In: *Proceedings of the Third International Conference on Very High Cycle Fatigue – VHCF-3*. Eds.: Sakai, T., Ochi, Y. Kusatsu, Society of Materials Science, Japan (JSMS) 2004, p. 633.
- [11] TOKAJI, K.—KO, H.-N.—NAKAJIMA, M.—ITOGA, H.: *Mater. Sci. Engng. A*, A345, 2003, p. 197.
- [12] MELANDER, A.—LARSSON, M.: *Int. J. Fatigue*, 15, 1993, p. 119.
- [13] LARSSON, M.—MELANDER, A.—NORDGREN, A.: *Mater. Sci. Techn.*, 9, 1993, p. 235.
- [14] MURAKAMI, Y.—YOKOYAMA, N. N.—NAGATA, J.: *Fatigue Fract. Engng. Mater. Struct.*, 25, 2002, p. 735.
- [15] MURAKAMI, Y.—NOMOTO, T.—UEDA, T.—MURAKAMI, Y.: *Fatigue Fract. Engng. Mater. Struct.*, 23, 2000, p. 893.
- [16] MURAKAMI, Y.—NOMOTO, T.—UEDA, T.—MURAKAMI, Y.: *Fatigue Fract. Engng. Mater. Struct.*, 23, 2000, p. 903.

- [17] MURAKAMI, Y.—NOMOTO, T.—UEDA, T.: *Fatigue Fract. Engng. Mater. Struct.*, 22, 1999, p. 581.
- [18] MURAKAMI, Y.—TAKADA, M.—TORIYAMA, T.: *Int. J. Fatigue*, 16, 1998, p. 661.
- [19] NISHIJAMA, S.—KANAZAWA, K.: *Fatigue Fract. Engng. Mater. Struct.*, 22, 1999, p. 601.
- [20] OCHI, Y.—MATSAMURA, T.—MASAKI, K.—YOSHIDA, S.: *Fatigue Fract. Engng. Mater. Struct.*, 25, 2002, p. 823.
- [21] SAKAI, T.—SATO, Y.—OGUMA, N.: *Fatigue Fract. Engng. Mater. Struct.*, 25, 2002, p. 765.
- [22] SHIINA, T.—NAKAMURA, T.—NOGUCHI, T.: In: *Proceedings of the Third International Conference on Very High Cycle Fatigue – VHCF-3*. Eds.: Sakai, T., Ochi, Y. Kusatsu, Kyoto Society of Materials Science, Japan (JSMS) 2004, p. 48.
- [23] SHIOZAWA, K.—LU, L.—ISHIHARA, S.: *Fatigue Fract. Engng. Mater. Struct.*, 24, 2002, p. 781.
- [24] SHIOZAWA, K.—LU, L.: *Fatigue Fract. Engng. Mater. Struct.*, 25, 2002, p. 813.
- [25] SHIOZAWA, K.—MORII, Y.—NISHINO, S.—LU, L.: *Fatigue Fract. Engng. Mater. Struct.*, 28, 2006, p. 1521.
- [26] TANAKA, K.—AKINIWA, Y.: *Fatigue Fract. Engng. Mater. Struct.*, 25, 2002, p. 775.
- [27] TANAKA, K.—AKINIWA, Y.—MIYAMOTO, N.: In: *Proceedings of the Third International Conference on Very High Cycle Fatigue – VHCF-3*. Eds.: Sakai, T., Ochi, Y. Kusatsu, Kyoto Society of Materials Science, Japan (JSMS) 2004, p. 56.
- [28] SOHAR, C. R.—BETZWAR-KOTAS, A.—GIERL, C.—WEISS, B.—DANNINGER, H.: *Int. J. Fatigue*, 30, 2008, p. 1137.
- [29] MARINES, I.—BIN, X.—BATHIAS, C.: *Int. J. Fatigue*, 25, 2003, p. 1101.
- [30] SOHAR, C. R.—BETZWAR-KOTAS, A.—GIERL, C.—WEISS, B.—DANNINGER, H.: *Int. J. Fatigue*, doi:10.1016/j.ijfatigue.2008.05.013.
- [31] BERNS, H.—TROJAHN, W.: *VDI-Z*, 127, 1985, p. 889.
- [32] BERNS, H.—LUEG, J.—TROJAHN, W.—WÄHLING, R.—WISELL, H.: *Powder Metall. Int.*, 19, 1987, p. 22.
- [33] FUKAURA, K.—YOKOYAMA, Y.—YOKOI, D.—TSUJII, N.—ONO, K.: *Met. Mat. Trans. A*, 35A, 2004, p. 1289.
- [34] MARSONER, S.—EBNER, R.—LIEBFAHRT, W.—JEGLITSCH, F.: *HTM*, 57, 2002, p. 283.
- [35] MARSONER, S.—EBNER, R.—LIEBFAHRT, W.: *BHM*, 148, 2003, p. 176.
- [36] MEURLING, F.—MELANDER, A.—TIDESTEN, M.—WESTIN, L.: *Int. J. Fatigue*, 23, 2001, p. 215.
- [37] SOHAR, CH. R.—BETZWAR-KOTAS, A.—GIERL, CH.—WEISS, B.—DANNINGER, H.: *Kovove Mater.*, 46, 2008, p. 197.